# Advanced reconstruction algorithms for electron tomography: From comparison to combination

B. Goris [a], T. Roelandts [b], K.J. Batenburg [b,c], H. Heidari Mezerji [a], S. Bals [a,*]

[a] EMAT, University of Antwerp, Groenenborgerlaan 171, B-2020 Antwerp, Belgium
[b] Vision Lab, University of Antwerp, Universiteitsplein 1, B-2610 Wilrijk, Belgium
[c] Centrum Wiskunde & Informatica, Science Park 123, NL-1098XG Amsterdam, The Netherlands

## ARTICLE INFO

*Keywords:*
Electron tomography
Total variation minimization
Discrete algebraic reconstruction technique
Reconstruction algorithm

## ABSTRACT

In this work, the simultaneous iterative reconstruction technique (SIRT), the total variation minimization (TVM) reconstruction technique and the discrete algebraic reconstruction technique (DART) for electron tomography are compared and the advantages and disadvantages are discussed. Furthermore, we describe how the result of a three dimensional (3D) reconstruction based on TVM can provide objective information that is needed as the input for a DART reconstruction. This approach results in a tomographic reconstruction of which the segmentation is carried out in an objective manner.

© 2012 Elsevier B.V. All rights reserved.

## 1. Introduction

Electron tomography is a technique that enables one to obtain a three dimensional (3D) reconstruction starting from of a tilt series of two dimensional (2D) projection images acquired using a transmission electron microscope (TEM). During the last decade, electron tomography has evolved into a standard technique for 3D characterization in material science [1]. Different TEM projection techniques can be extended successfully to 3D, e.g. bright field TEM [2], high angle annular dark field (HAADF) scanning transmission electron microscopy (STEM) [3], energy filtered TEM [4,5], dark field TEM [6], annular dark field TEM [7], and electron holography [8]. After alignment of the projection images, the reconstruction of a 3D volume out of its 2D projections is typically carried out using a weighted backprojection (WBP) or an iterative reconstruction algorithm. The simultaneous iterative reconstruction technique (SIRT) [9] is nowadays widely used.

It is known that a 3D reconstruction might suffer from so-called "missing wedge" artefacts. A gap in the available angular range is indeed often unavoidable because of the limited space between the polepieces of the objective lens in the electron microscope and shadowing effects at high tilt angles. The quality of the reconstruction can furthermore suffer from the fact that for specific materials only a limited number of projections can be acquired due to electron beam damage. Recently, several alternative reconstruction algorithms have been developed. These algorithms exploit additional knowledge about the original object during the reconstruction. In this manner, both the effect of the missing wedge and the limited number of projections can be minimized leading to reconstructions with a higher fidelity in comparison to classical iterative reconstruction algorithms.

The discrete algebraic reconstruction technique (DART) uses prior knowledge concerning the discrete number of grey levels of the reconstructed object [10,11]. Beside reduction of artefacts, this algorithm has the additional advantage that thresholding is already applied during the reconstruction, leading to a more straightforward quantification of the reconstruction. DART was successfully used for the 3D characterization of C nanotubes containing catalytic CuO particles [12], zeolite materials [13], and several other types of nanoparticles [10,14]. A different kind of prior knowledge is exploited when using total variation minimization (TVM) based reconstruction algorithms. Here, it is assumed that the object that needs to be reconstructed has a sparse gradient at the nanometer scale. This is a good assumption because, for objects at the nanoscale, it is often valid to assume that boundaries between different compounds are sharp, leading to a sparse gradient of the object. This is illustrated in Fig. 1, in which a phantom object together with its gradient image is shown. Although the image in Fig. 1a is not sparse, Fig. 1b shows that the gradient is sparse. This technique was recently used for 3D reconstructions of FeO nanoparticles [15], Au nanoparticles, PbSe–CdSe core/shell nanoparticles and Pb nanoparticles in a Si needle [16].

These novel reconstruction algorithms all have specific requirements, advantages and disadvantages. In this work, we will make a comparative study of the different reconstruction algorithms. In addition, we will combine the different algorithms in order to further improve the results.

* Corresponding author.
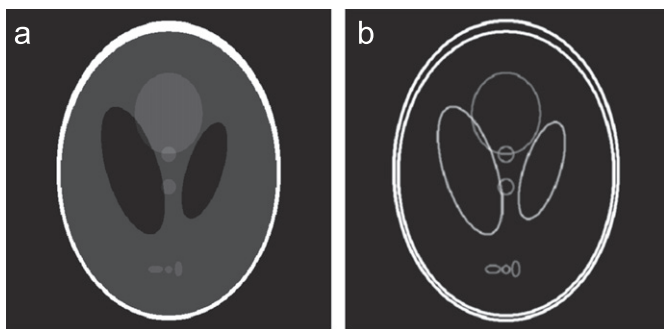  *E-mail address:* sara.bals@ua.ac.be (S. Bals).

**Fig. 1.** (a) Shepp Logan phantom object and its gradient image (b). It can be seen that the gradient image is a sparse representation of the original object.

## 2. Advanced reconstruction algorithms

The basics of electron tomography can be explained based on 1D projections of a 2D object. The extension to a 3D object is straightforward since this object can be regarded as a set of 2D slices. For a tomographic tilt series, $N$ projections (each containing $k$ pixels) are acquired at tilt angles $\{\theta_1, \theta_2, \ldots, \theta_N\}$ from a discretized object $f(u,v)$ with a width $w$ and a height $h$. As noticed from Fig. 2, the projections can be seen as a matrix multiplication between a projection matrix and the imaged object:

$$Ax = b. \tag{1}$$

Here, $b$ is a vector representing the projections, $x$ is a vector that represents the imaged object and $A$ is the projection matrix that is defined in such a way that the element $a_{i,j}$ represents the contribution of pixel $i$ to projection ray $j$. To create a tomographic reconstruction, the unknown vector $x$ has to be determined from the measurements $b$. This is not straightforward due to the limited number of projections. As a result, the tomographic problem is underdetermined. Noise and other errors in the measured tilt series will also hamper the reconstruction of the imaged object. The three reconstruction algorithms that are used in this study are SIRT [9], a TVM based reconstruction algorithm [16] and DART [10].

### 2.1. Simultaneous iterative reconstruction technique

SIRT is a reconstruction technique that is based on the Riemann backprojection principle [9]. Our SIRT implementation will start from a first reconstruction obtained by a regular backprojection. This reconstruction is re-projected along the original tilt angles that were used to acquire the experimental projection images. The re-projections are all compared simultaneously to the original projections. The difference between both is calculated and is referred to as the "projection difference". A reconstruction of these differences is then calculated by performing an unfiltered backprojection of the differences, and added to the previous reconstruction. This process is iterated until convergence is reached. In practice, this method will converge after approximately 20–30 iterations [17]. The SIRT algorithm that is used in the remainder of this work is implemented in Matlab to simplify comparison with the other reconstruction algorithms which are also carried out through Matlab.

### 2.2. Total variation minimization reconstruction algorithm

Compressive sensing is a field in image processing that is specialized in finding a solution to a set of ill-posed linear equations that has a sparse representation in some basis [18–21]. In electron tomography of nanostructured materials, it is often valid to assume
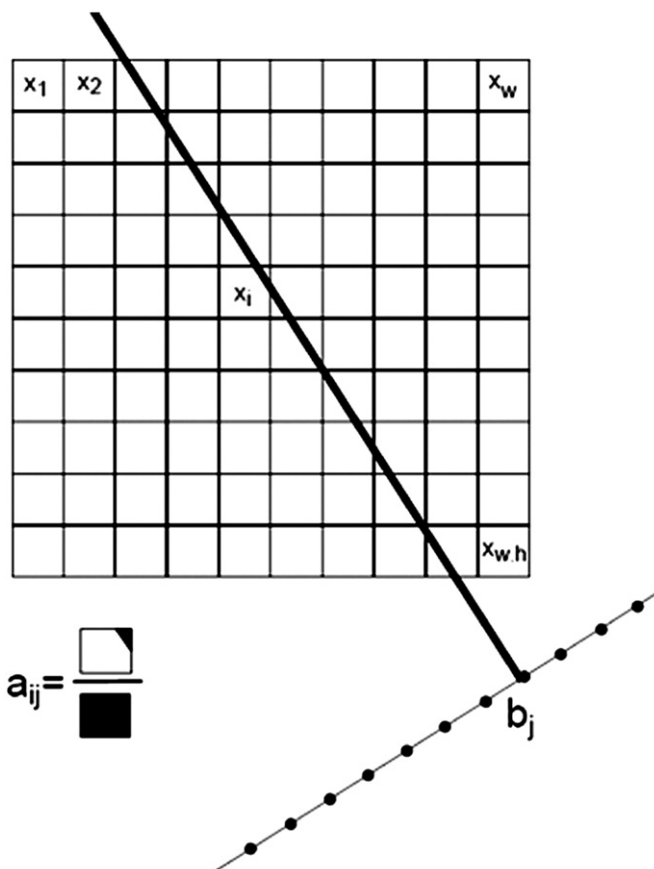


**Fig. 2.** Projection geometry for tomographic experiment. The vector $x$ represents the imaged object with dimensions $w \times h$. The element $a_{ij}$ of the projection matrix $A$ equals the contribution of element $x_i$ to projection ray $b_j$.

that the investigated object is not sparse when represented on a standard pixel basis, but that its boundary, representing the interface between different compositions, is sparse. This sparsity assumption can be incorporated in a tomographic reconstruction algorithm by simultaneously minimizing the projection distance and the total variation (i.e. the norm of the discrete gradient) of the reconstruction object:

$$\hat{x} = \arg\min_x \left[ TV(x) + \frac{\mu}{2} \|Ax - b\|_2^2 \right]. \tag{2}$$

Here, $TV(x)$ represents the total variation of the object and $\mu$ is a regularization parameter indicating the importance of both terms in the equation. The last term $\|Ax - b\|_2^2$ represents the projection distance which is a measure for the correspondence between the experimental projection images and the reprojections of the (intermediate) 3D reconstruction. This equation minimizes both the projection distance and the total variation and therefore results in a reconstruction which approximately satisfies the projection data and has a low total variation. Due to the sparsity exploited during the reconstruction algorithm, this approach yields reconstructions in which missing wedge artefacts are reduced.

### 2.3. Discrete algebraic reconstruction algorithm

DART is an iterative algorithm that incorporates prior knowledge concerning the different grey levels of the imaged object. This extra knowledge is implemented by combining a continuous iterative reconstruction algorithm (such as SIRT) with discretization steps. The method starts by calculating a conventional SIRT reconstruction which is subsequently thresholded. The result is

then iteratively improved by applying a sequence of *boundary reconstruction* steps, intertwined with segmentation steps. In each iteration, the current grey level image is first segmented by thresholding, to obtain a reconstruction that contains only grey levels from a pre-determined set. In this segmented image, the set of boundary pixels is determined, which consists of all pixels that are adjacent to pixels from another segmentation class. These boundary pixels are then updated by the continuous iterative method, while keeping the remainder of the pixels fixed at their segmented grey levels. In this way, the number of unknowns (i.e., the boundary pixels) is strongly reduced, resulting in a less-underdetermined reconstruction problem. In this way, the accuracy of the boundary is improved, which results in an improved segmentation in the next DART iteration. It has been shown that DART yields reconstructions that contains less (missing wedge) artefacts in comparison to a SIRT reconstruction. An additional advantage is that the reconstruction is already segmented leading to a straightforward quantification of the reconstructed dataset. A prerequisite for DART is that the expected number of grey values, as well as the *actual grey levels* corresponding with the different compositions of the sample, should be known. For the implementation of the DART algorithm, both the grey values of the reconstructed object and the threshold values that are used in the reconstruction are needed as well as the percentage of non-boundary pixels that are fixed to their previous grey level. This percentage can be adjusted according to the noise present in the projection images of the experimental tilt series.

## 3. Au nanoparticles

The first test object that is used for the comparison between the different reconstruction algorithms consists of Au nanoparticles deposited on an amorphous C support layer. A tomographic tilt series is acquired at tilt angles ranging from $-70°$ to $+78°$ with a $2°$ tilt increment in HAADF-STEM mode. The annular detector excludes all electrons that have scattered to a semi-angle lower than 54 mrad to avoid unwanted diffraction contrast. One of the 2D projections is presented in Fig. 3. The acquisition is performed using a TecnaiG2 microscope operated by the auto-mated FEI Xplore3D™ Tomography Suite software. The magnification that is used corresponds to a pixel size of 0.38 nm. To compensate for cupping artefacts caused by non-linear thickness effects in HAADF-STEM tomography, the measured intensities are
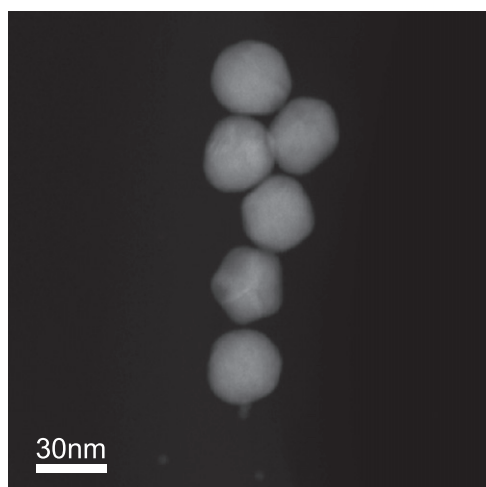
calibrated with respect to the incoming electron beam [22]. This calibration implies that we transform the measured intensity $I$ to a signal that is linear to the thickness $t$ of the sample through the
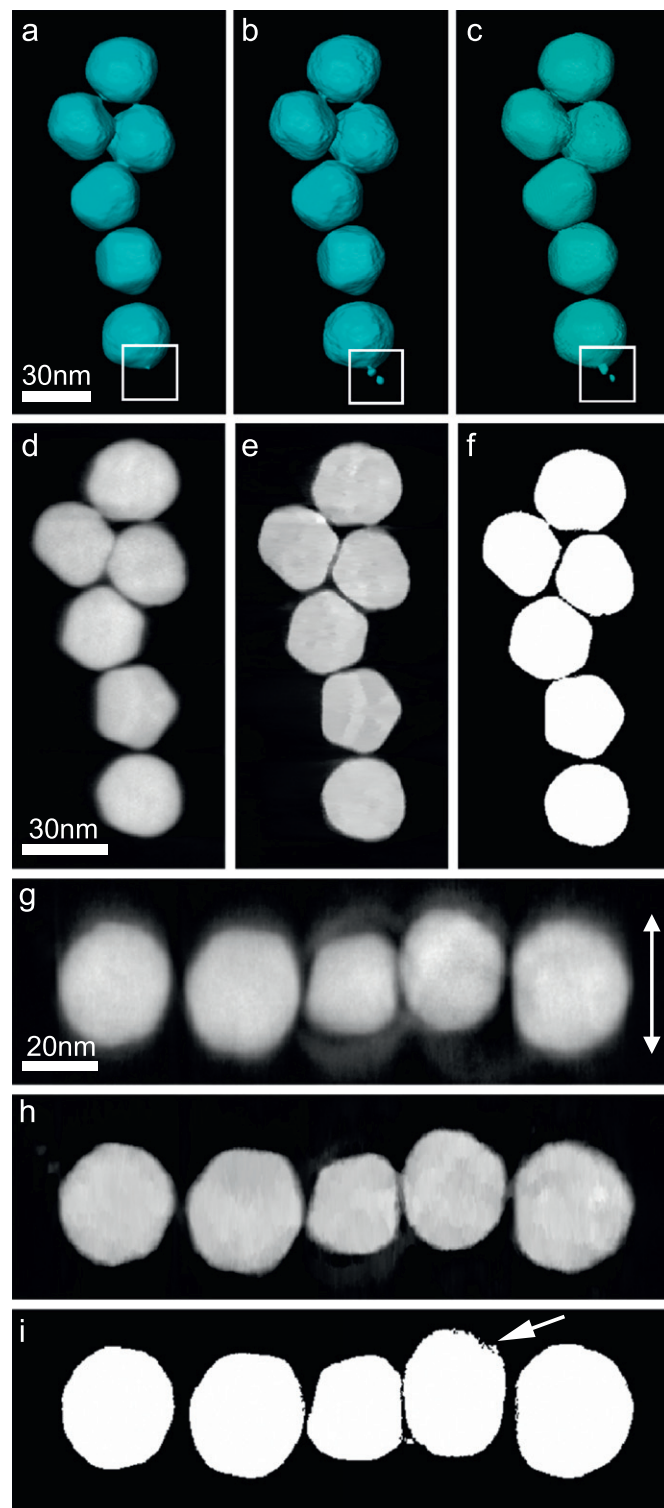


**Fig. 4.** Reconstruction of Au nanoparticles with a diameter of approximately 30 nm. (a), (b) and (c) present isosurface renderings of a SIRT, a TVM and a DART reconstruction respectively. From the orthoslices through the SIRT reconstruction (d and g), it can be seen that an elongation along the direction of the missing wedge is present. Orthoslices through the TVM reconstruction (e and h) reveal that the boundary facets of the nanoparticles are easier to determine in this reconstruction in comparison to the SIRT reconstruction. The DART reconstruction (f and i) has the advantage that segmentation becomes much easier since thresholding is already applied during the algorithm.



**Fig. 3.** HAADF-STEM projection of cluster of Au nanoparticles with an average diameter of 30 nm.

transformation formula:

$$\mu t = -\log\left(1 - \frac{I}{I_0}\right). \tag{3}$$

Here, $I_0$ corresponds to the intensity of the incoming electron beam and $\mu$ is equal to the inverse of the mean free path of the electrons. This methodology was recently proposed in [22]. Alignment of the tilt series is performed using cross-correlation available in the Inspect3D software.

### 3.1. SIRT reconstruction

First, a SIRT reconstruction of the tilt series is calculated. An isosurface rendering together with two orthogonal slices through the reconstruction are presented in Fig. 4a, d and g respectively. Orthoslices through the reconstruction along the direction of the missing wedge (Fig. 4g) reveal an elongation, which is indicated by the white arrow. Such elongation is expected for a SIRT reconstruction based on the tilt range used in this study. It must be noted that the small Au particles (encircled in Fig. 4a–c) having a diameter of 5 nm cannot be observed in the SIRT reconstruction, although they are present in all projection images of the tilt series.

### 3.2. TVM reconstruction

Next, a TVM reconstruction is performed using the same tilt series. The regularization parameter $\mu$ that describes the weight of the variation regularization term equals 0.5. The result of this reconstruction is presented in Fig. 4b, e and h. Fig. 4b corresponds to an isosurface rendering and Fig. 4e and h shows orthoslices through the reconstruction. From the isosurface rendering, it appears that the small Au particles (encircled in Fig. 4b) are reconstructed well. From the orthoslices, it can be seen that the elongation along the direction of the missing wedge is reduced in comparison to the SIRT reconstruction. Moreover, also the side facets that compose the morphology of the Au nanoparticles are better defined in the TVM reconstruction. In both the SIRT and TVM reconstruction, intensity variations in the nanoparticles can be observed, which are caused by residual diffraction contrast in the original projections.

### 3.3. DART reconstruction

Finally, a DART reconstruction of the Au nanoparticles is created. The intensity values used in this DART reconstruction are obtained by inspecting the grey values of the previous SIRT and TVM reconstructions. An isosurface rendering of the reconstruction is shown in Fig. 4c and Fig. 4f and i presents two orthoslices through the reconstruction. For the isosurface renderings, the same threshold values are used for the SIRT, TVM and DART reconstructions. No elongation in the direction of the missing wedge is observed and it can be seen that the side facets of the nanoparticles are clearly defined. Also for DART, the smallest particles can be observed in the isosurface rendering of the final reconstruction. An extra advantage of this DART reconstruction is that the segmentation is carried out during the reconstruction algorithm. It must be noted that the intensity variations in the nanoparticles do not appear in the DART reconstruction due to the specific nature of the algorithm. However, the residual diffraction contrast that is present in the projections may hamper the correct estimation of the boundaries leading to small artefacts as indicated by a white arrow in Fig. 4i.

## 4. CdSe/PbSe core/shell nanoparticles

The second test sample contains PbSe/CdSe core/shell nanoparticles having an average diameter of 9 nm and being dispersed on a C support. A tilt series of a particle assembly is acquired with an angular range from $-70°$ to $+78°$ and a tilt increment of $2°$ in HAADF-STEM mode. A semi-inner collection angle of 56 mrad is used to avoid diffraction contrast. The acquisition is performed at a cubed FEI TITAN microscope using a Fischione tomography tilt holder operated by the FEI Xplore3D software. The pixel size used during the acquisition of the tilt series equals 1.36 nm. This is larger in comparison to the full width half maximum (FWHM) of the STEM probe ($\pm 1.2$ Å). This means that the pixel size will be the limiting factor in the reconstruction. The projection acquired at $0°$ tilt angle is presented in Fig. 5a. High resolution HAADF-STEM images confirming the core–shell structure are presented in Fig. 5b and c. Alignment of the tilt series is done by a combination
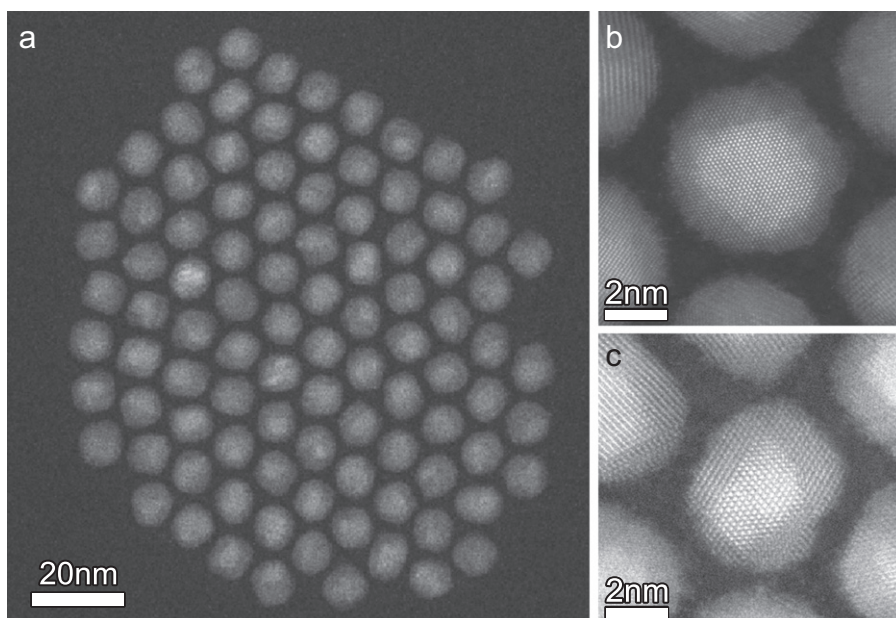


**Fig. 5.** (a) HAADF-STEM projection of cluster of PbSe–CdSe nanoparticles with an average diameter of 9 nm. (b) and (c) show high resolution HAADF-STEM images confirming the core–shell structure of the nanoparticles.

of cross-correlation available in the FEI Inspect3D software and a manual alignment using the IMOD software [23]. The reconstruction of Au nanoparticles suggests that a DART reconstruction yields the best reconstruction since missing wedge artefacts are absent and the reconstruction is already segmented. However, it must be noted that for DART reconstructions of samples containing multiple chemical compositions, it is not straightforward to determine the grey levels and the threshold values that are needed as input for the reconstruction. Also the regularization parameter $\mu$ for the TVM algorithm becomes more difficult to

determine. The only reconstruction that can be achieved without using any prior knowledge is a SIRT reconstruction.

### 4.1. SIRT reconstruction

For the SIRT reconstruction, a voltex rendering and two orthoslices through the reconstruction are shown in Fig. 6a, d and g respectively. In this last slice, showing the direction along the missing wedge, a clear elongation of the core/shell nanoparticles can be seen together with other missing wedge artefacts.
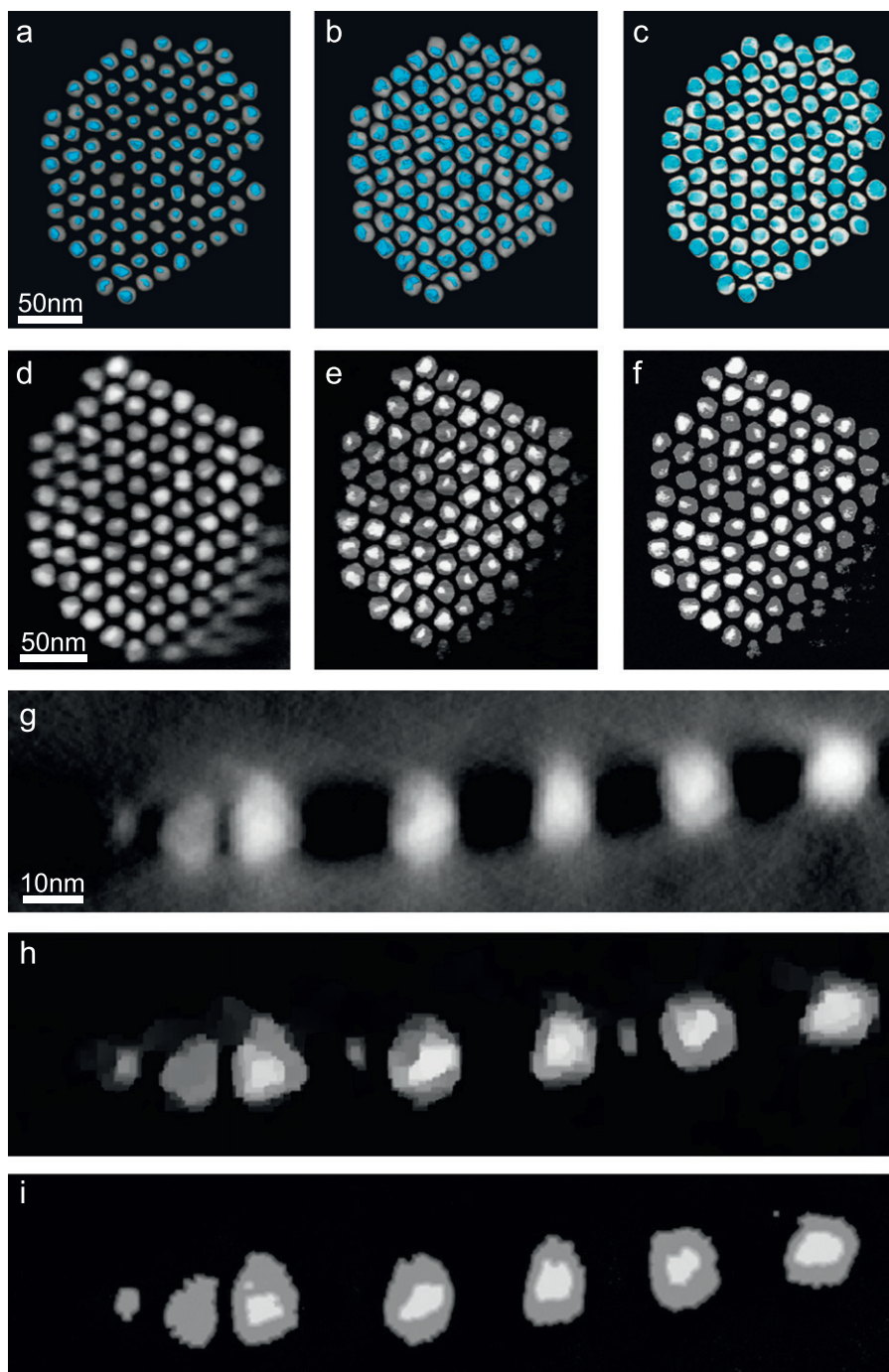


**Fig. 6.** Visualizations of reconstructions of cluster of core/shell nanoparticles with an average diameter of 9 nm. (a), (b) and (c) show a 3D rendering of the SIRT, TVM and DART reconstructions respectively. Slices through the SIRT reconstruction (d and g) show an elongation in the direction of the missing wedge. This elongation is reduced in both the slices through the TVM (e and h) and the DART (f and i) reconstructions. Furthermore, the DART reconstruction has the advantage that thresholding is already applied in the reconstruction algorithm leading to a straightforward quantification of the dataset. In the last slice through the TVM reconstruction (h), small regions with a higher intensity are visible between the core/shell nanoparticles. This is caused because the slice also intersects the beginning of a second row of nanoparticles.
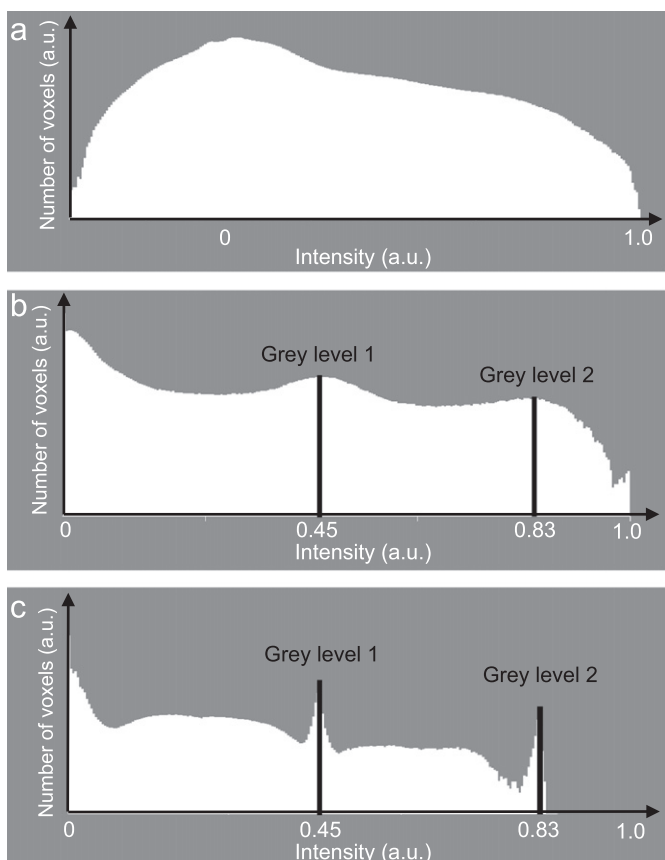
**Fig. 7.** Grey level histograms of the SIRT (a), TVM (b) and DART (c) reconstruction. From the TVM and the DART reconstruction, the grey levels corresponding to the core and to the shell can be recognized. This is impossible from the first SIRT reconstruction where also negative values are present as a consequence of noise and other reconstruction artefacts.

The grey level histogram of the reconstruction is presented in Fig. 7a and indicates that there is not a clear grey level corresponding to the core and the shell of the particles. This is an indication that segmentation of the reconstructed dataset will be far from straightforward. Although negative intensity values have no physical meaning for electron tomography reconstructions based on HAADF-STEM imaging, they are often observed. Such negative values are the result of a combination of noise and various reconstruction artefacts.

### 4.2. TVM reconstruction

Also a TVM reconstruction of the nanoparticles is created. For a dataset containing different chemical compositions and grey levels, the regularization parameter $\mu$ becomes more crucial. A very high value of $\mu$ will lead to a reconstruction resembling a SIRT reconstruction. On the other hand, an underestimation of the value of $\mu$ results in a reconstruction where noise and artefacts are reduced, but high frequency details are lost as well. A TVM reconstruction of a 2D slice through the core/shell nanoparticles is shown in Fig. 8 where different values for the regularization parameter $\mu$ are used. The images in Fig. 8 suggest that $\mu = 0.5$ provides a good trade-off between the level of high frequency details and artefact reduction in the reconstruction. An estimation of the reconstruction that was expected, can be determined from the previous SIRT reconstruction where no prior knowledge is required. A 3D visualization of the TVM reconstruction is presented in Fig. 6b and two orthoslices through the reconstruction are shown in Fig. 6e and h. From these slices, it is clear that missing
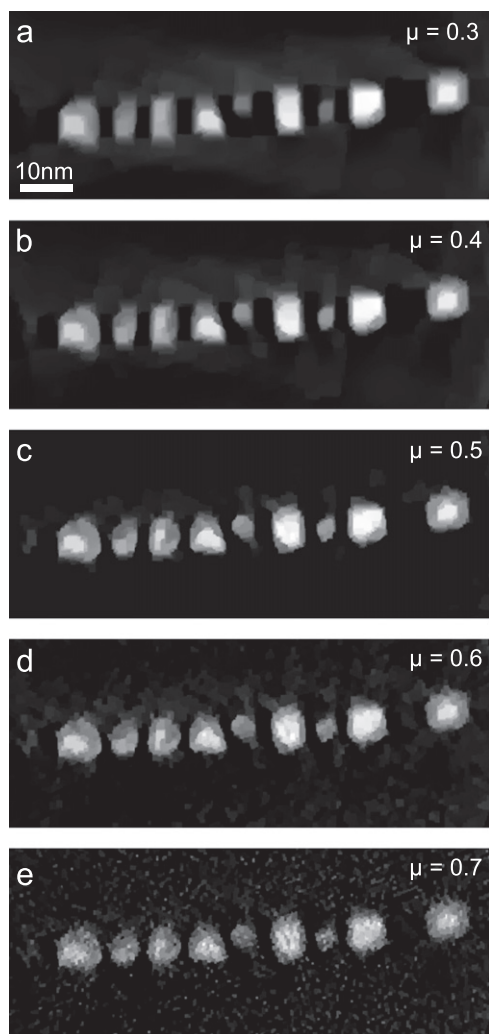


**Fig. 8.** TVM reconstruction of slice through core/shell nanoparticles for different regularization parameters $\mu$. It can be seen that $\mu = 0.5$ provides a good trade-off between the level of high frequency details and artefact reduction in the reconstruction.

wedge artefacts are reduced in comparison to a SIRT reconstruction. From the orthoslice shown in Fig. 6h, it can be seen that the pixel size is indeed the limiting resolution factor in this reconstruction. Furthermore, segmentation and therefore quantification becomes easier since the grey levels of the different chemical components are more pronounced in this reconstruction compared to a SIRT reconstruction. This can be seen in the histogram through the reconstruction displayed in Fig. 7b. From the grey level histogram of the reconstruction, it is clear that the grey level of the shell corresponds to 0.45 and the grey level of the core to 0.83. Negative intensity values are absent in the histogram of the reconstruction because during the TVM reconstruction, an additional restriction is used forcing the intensity values to be positive.

### 4.3. DART reconstruction

Whereas it is difficult to compare the quality of reconstructions of experimental datasets, the previous dataset of Au nanoparticles suggested that DART provides a reconstruction with a superior quality in comparison to SIRT and TVM. However, an estimation of the grey levels is necessary for the reconstruction and this is not always straightforward in case the investigated sample contains different chemical compositions. Although the estimation of these grey levels can partially be automated in certain cases, obtaining the

correct values can be particularly troublesome if a grey level occurs only in small regions, such as the cores in the present dataset [24]. As an example, DART reconstructions of a slice through the core/shell nanoparticles where different grey values are used as input are presented in Fig. 9. The threshold values that are used for the reconstruction are always chosen as the average between the two grey levels. From this figure, it can be seen that using different grey levels as input in the algorithm results in relatively large differences in the reconstructed slices. When inspecting the reconstructed slices in more detail, it can be seen that a grey value of 0.45 for the shell and 0.83 for the core provides the best result. A convenient way to determine these grey values is by inspecting the grey level histogram of the TVM reconstruction. This histogram is presented in Fig. 7b and it can be seen that the grey levels correspond indeed to 0.45 (shell) and 0.83 (core). These values can now be used as the input values for a full DART reconstruction. A 3D rendering of the resulting DART reconstruction is shown in Fig. 6c and orthoslices are displayed in Fig. 6f and i. For the isosurface renderings in Fig. 6a, b and c, the same threshold value is used for the visualization of the SIRT, the TVM and the DART reconstruction. From these visualizations of the reconstruction, it can be seen that a DART reconstruction is again free of missing wedge artefacts and has the advantage that thresholding is already applied in the algorithm leading to a more quantitative result than a TVM or SIRT reconstruction. A specific implementation of the DART algorithm can be used that results in a reconstruction with a
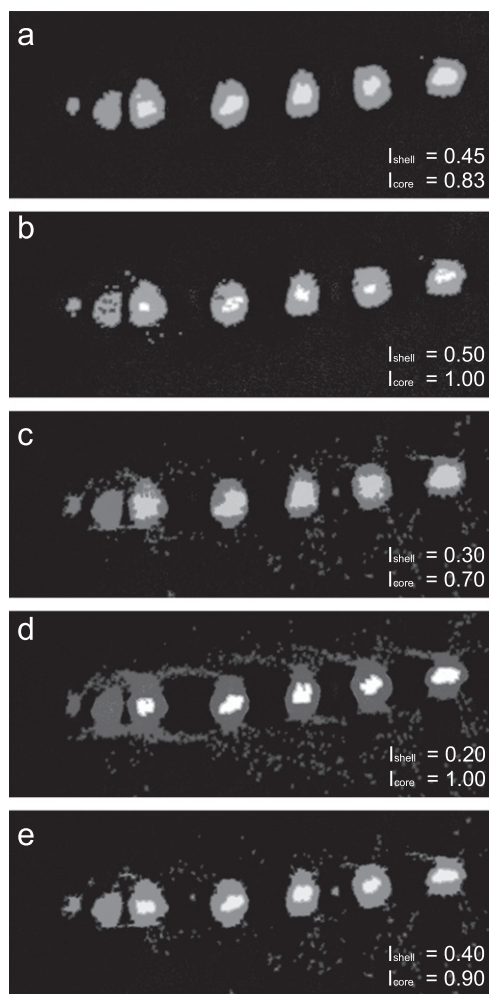
better resolution than the pixel size of the projection images [25]. The histogram of the resulting DART reconstruction is shown in Fig. 7c. It must be noted that this histogram is not completely discrete because our implementation of DART does not end with a thresholding step leading to multiple grey levels at the boundaries of the reconstruction. An additional segmentation step has no visual influence on the reconstruction, but will result in a discrete histogram with only three nonzero intensities. Since we were unable to separate the intensities of the C support and the vacuum in the TVM reconstruction, the Csupport is not taken into account in the discretization process of the DART reconstruction. Using an additional grey level that corresponds to the amorphous C support does not improve the quality of the reconstruction.

## 5. Discussion

Three different tomographic reconstruction algorithms (SIRT, TVM and DART) are applied to two different experimental datasets. First, a reconstruction is made from a tilt series of Au nanoparticles with a diameter of approximately 30 nm. Based on the reconstructions, it is shown that all the algorithms are capable of creating a fairly good reconstruction of the morphology of the nanoparticles. A TVM reconstruction has the advantage that missing wedge artefacts are reduced in comparison to a SIRT reconstruction. The major advantage of a DART reconstruction in comparison to SIRT and TVM is that the segmentation is applied during the reconstruction leading to an easier quantification of the reconstructed dataset. The reconstruction of a second dataset of CdSe/PbSe core/shell nanoparticles with an average diameter of 9 nm shows that combining the information obtained from the reconstructions can lead to a beneficial situation. From a first SIRT reconstruction, the main morphology of the reconstructed dataset can be estimated and based on this knowledge, the regularization parameter $\mu$ can be determined that is needed as an input for a TVM reconstruction. This TVM reconstruction is easier to segment in comparison to a SIRT reconstruction leading to an optimized estimation of the grey levels necessary for a DART reconstruction where quantitative information can easily be obtained. Whereas this method results in an objective determination of the grey levels that are needed as an input for a DART algorithm, we believe that further progress can be made in optimizing the threshold values that are needed as well. This approach where the result of one reconstruction provides the input of a second reconstruction is shown in the flowchart presented in Fig. 10.
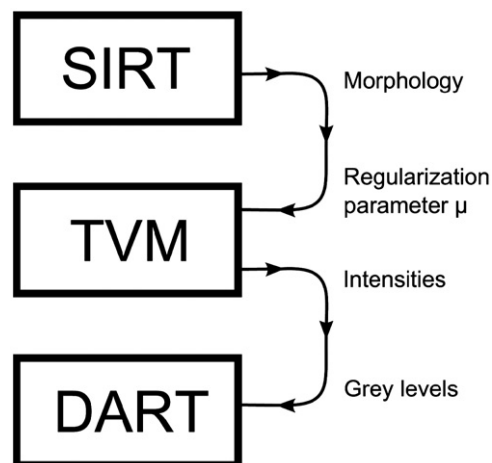


**Fig. 9.** DART reconstruction of slice through core/shell particles with different threshold values. From these reconstructions, it can be seen that large differences are present in the reconstructed slice based on the grey levels that are used as input values.



**Fig. 10.** Flowchart of tomographic reconstruction algorithms. This scheme indicates that the result of one reconstruction algorithm can provide the required input for the following reconstruction.

## 6. Conclusions

In this work, three tomographic reconstruction algorithms are compared and the advantages and disadvantages are discussed. Furthermore, it is shown that a SIRT reconstruction can serve as a starting point for determining the correct regularization parameter in a TVM reconstruction. Next, the thresholded intensities from this TVM reconstruction serve as the grey values that are required in a DART reconstruction. By using this scheme, a reconstruction can be obtained where missing wedge artefacts are reduced and from which quantitative information can be extracted.

## Acknowledgement

## References

[1] P.A. Midgley, R. Dunin-Borkowski, Electron tomography and holography in materials science, Nature Materials 8 (2009) 271–280.

[2] A. Koster, U. Ziese, A. Verkleij, A. Janssen, K. De Jong, Three-dimensional transmission electron microscopy: a novel imaging and characterization technique with nanometer scale resolution for materials science, Journal of Physical Chemistry B 104 (2000) 9368–9370.

[3] P.A. Midgley, M. Weyland, 3D electron microscopy in the physical sciences: the development of z-contrast and eftem tomography, Ultramicroscopy 96 (2003) 413–431.

[4] G. Mobus, R. Doole, B. Inkson, Spectroscopic electron tomography, Ultramicroscopy 96 (2003) 433–451.

[5] B. Goris, S. Bals, W. Van den Broek, J. Verbeeck, G. Van Tendeloo, Exploring different inelastic projection mechanisms for electron tomography, Ultramicroscopy 111 (2011) 1262–1267.

[6] J. Barnard, J. Sharp, J. Tong, P. Midgley, High-resolution three-dimensional imaging of dislocations, Science 303 (2006) 319.

[7] S. Bals, G. Van Tendeloo, C. Kisielowski, A new approach for electron tomography: annular dark-field transmission electron microscopy, Advanced Materials 18 (2006) 892–895.

[8] D. Wolf, A. Lubk, H. Lichte, H. Friedrich, Towards automated electron holographic tomography for 3d mapping of electrostatic potentials, Ultramicroscopy 110 (2010) 390–399.

[9] P. Gilbert, Iterative methods for the three-dimensional reconstruction of an object from projections, Journal of Theoretical Biology 36 (1972) 105–107.

[10] K. Batenburg, S. Bals, J. Sijbers, C. Kübel, P. Midgley, J. Hernandez, U. Kaiser, E.R. Encina, E. Coronado, G. Van Tendeloo, 3D imaging of nanomaterials by discrete tomography, Ultramicroscopy 109 (2009) 730–740.

[11] K. Batenburg, J. Sijbers, Dart: a practical reconstruction algorithm for discrete tomography, IEEE Transactions on Image Processing 20 (2011) 2542–2553.

[12] S. Bals, K. Batenburg, J. Verbeeck, J. Sijbers, G. Van Tendeloo, Quantitative three-dimensional reconstruction of catalyst particles for bamboo-like carbon nanotubes, Nano Letters 7 (2007) 3669–3674.

[13] S. Bals, K. Batenburg, D. Liang, O. Lebedev, G. Van Tendeloo, A. Aerts, J. Martens, C. Kirschhock, Quantitative three-dimensional modeling of zeotile through discrete electron tomography, Journal of the American Chemical Society 131 (2009) 4769–4773.

[14] S. Turner, M. Tavernier, G. Huyberechts, E. Biermans, S. Bals, K. Batenburg, G. Van Tendeloo, Assisted spray pyrolysis production and characterisation of ZnO nanoparticles with narrow size distribution, Journal of Nanoparticle Research 12 (2010) 615–622.

[15] Z. Saghi, D. Holland, R. Leary, A. Falqui, G. Bertoni, A. Sederman, L. Gladden, P. Midgley, Three-dimensional morphology of iron oxide nanoparticles with reactive concave surfaces. a compressed sensing-electron tomography (CS-ET) approach, Nano Letters 11 (2011) 4666–4673.

[16] B. Goris, W. Van den Broek, K. Batenburg, H. Mezerji, S. Bals, Electron tomography based on a total variation minimization reconstruction technique, Ultramicroscopy 113 (2012) 120–130.

[17] H. Mezerji, W. Van den Broek, S. Bals, A practical method to determine the effective resolution in incoherent experimental electron tomography, Ultramicroscopy 111 (2011) 330–336.

[18] D. Donoho, For most large undetermined systems of linear equations, the minimal $l^1$-norm solution is also the sparsest solution, Communications on Pure and Applied Analysis 59 (2006) 797–829.

[19] D. Donoho, Compressed sensing, IEEE Transactions on Information Theory 52 (2006) 1289–1306.

[20] E. Candes, J. Romberg, T. Tao, Stable signal recovery from incomplete and inaccurate measurements, Communications on Pure and Applied Analysis 59 (2008) 1207–1223.

[21] E. Candes, M. Wakin, An introduction to compressive sampling, IEEE Signal Processing Magazine 25 (2008) 21–30.

[22] W. Van den Broek, A. Rosenauer, B. Goris, G. Martinez, S. Bals, S. Van Aert, D. Van Dyck, Correction of non-linear thickness effects in electron tomography, Ultramicroscopy 116 (2012) 8–12.

[23] J. Kremer, D. Mastronarde, J. McIntosh, Computer visualization of three-dimensional image data using imod, Journal of Structural Biology 116 (1996) 71–76.

[24] K. Batenburg, W. van Aarle, J. Sijbers, A semi-automatic algorithm for grey level estimation in tomography, Pattern Recognition Letters 32 (2011) 1395–1405.

[25] W. Van Aarle, G. Van Gompel., K. Batenburg, E. Vande Casteele, J. Sijbers, A 3-dimensional discrete tomography approach for superresolution micro-CT images: application to foams, in: F. Noo (Ed.), The First International Conference on Image Formation in X-ray Computed Tomography, 2010, pp. 45–48.